

Understanding the Role of Organic Hole Transport Layers on Pinhole Blocking and Performance Improvement in Sb_2Se_3 Solar Cells

Thomas P. Shalvey, Christopher H. Don, Leon Bowen, Tim D. Veal, and Jonathan D. Major*

Sb_2Se_3 is an emerging semiconductor which has shown promise for low-cost photovoltaic applications. After successive record-efficiencies using a range of device structures, spiro-OMeTAD has emerged as the default hole transport material (HTM), however, the function of HTM layers remains poorly understood. Here, thin-film Sb_2Se_3 solar cells are fabricated with which three organic HTM layers - namely P3HT, PCDTBT, and spiro-OMeTAD are investigated. By comparing these against one another, and to a reference device, their role in the device stack are clarified. These organic HTM layers are found to serve a dual purpose, increasing both the average and peak efficiency by simultaneously blocking pinholes and improving the band alignment at the back contact, with marginal differences in performance between the different HTMs. This produced a champion device of 7.44% using P3HT, resulting from an improvement in all performance parameters. A more complex processing route, run-to-run variability, and lower overall device performance compared to the other organics challenge the assumption that spiro-OMeTAD is the optimal HTM for Sb_2Se_3 devices. A Schottky barrier at the Au- Sb_2Se_3 contact despite the deep work function of gold implies Fermi level pinning due to a defective interface, which each of the organic HTMs are equally capable of alleviating.

the past decade. Sb_2Se_3 has a high absorption coefficient,^[1] contains relatively non-toxic and abundant constituent elements,^[2] and does not suffer from stability issues observed in other solar technologies.^[3] A stereochemically active Sb 5s lone pair^[4] may instil a degree of defect tolerance to Sb_2Se_3 ,^[5] and results in a 1D orthorhombic *Pbnm* crystal structure whereby nano-ribbons are held together by van der Waals bonds. This is thought to result in benign grain boundaries^[6] and enhanced conductivity along the covalently bonded [001] direction. Furthermore, alloying with sulphur to produce $\text{Sb}_2(\text{S},\text{Se})_3$ allows the band gap to be varied between ≈ 1.2 – 1.7 eV for optimal spectral response, which has led to record device efficiencies of 10.57% and 10.75% for Sb_2Se_3 and $\text{Sb}_2(\text{S},\text{Se})_3$ respectively.^[7,8] These properties, combined with compatibility with high throughput physical vapor deposition methods^[9] offers the potential for large-scale, low-cost renewable electricity.

1. Introduction

Sb_2Se_3 based thin film solar cells are an emergent technology which have seen rapid improvements in device efficiency over

Antimony chalcogenide (Sb_2X_3) solar cells can be grown in both substrate and superstrate configuration, and both structures have produced high efficiency (>10%) devices. However, the superstrate device structure has been more commonly reported in the literature, and is used in the current record efficiency Sb_2Se_3 ,^[7] $\text{Sb}_2(\text{S},\text{Se})_3$,^[8] and Sb_2S_3 devices.^[10] The superstrate device structure is also well suited for studying hole extraction in Sb_2X_3 solar cells, since the back contact is deposited as the final processing step and is therefore easily controlled and remains accessible for measurement. In contrast, the back contact is buried at the bottom of the device stack for substrate devices, and will be affected by subsequent processing steps. Superstrate devices typically consist of Sb_2Se_3 deposited onto either CdS or TiO_2 window layers, followed by a metallic contact, which is almost always gold (see Figure 1e). In many instances, a *p*-type hole transporting material (HTM) is included between the Sb_2Se_3 layer and the metal contact to aid charge extraction, such as PbS quantum dots, amorphous MnS or a variety of organic semiconductors.^[11–13] Organic HTMs are particularly attractive owing to their ease of use and wide availability. Spiro-OMeTAD has been studied extensively for other solar

T. P. Shalvey, C. H. Don, T. D. Veal, J. D. Major
Stephenson Institute for Renewable Energy
Department of Physics
University of Liverpool
Liverpool L69 7ZF, UK
E-mail: jonmajor@liverpool.ac.uk

L. Bowen
Department of Physics
University of Durham
Durham DH1 3LE, UK

The ORCID identification number(s) for the author(s) of this article can be found under <https://doi.org/10.1002/admi.202400394>

© 2024 The Author(s). Advanced Materials Interfaces published by Wiley-VCH GmbH. This is an open access article under the terms of the [Creative Commons Attribution](#) License, which permits use, distribution and reproduction in any medium, provided the original work is properly cited.

DOI: 10.1002/admi.202400394

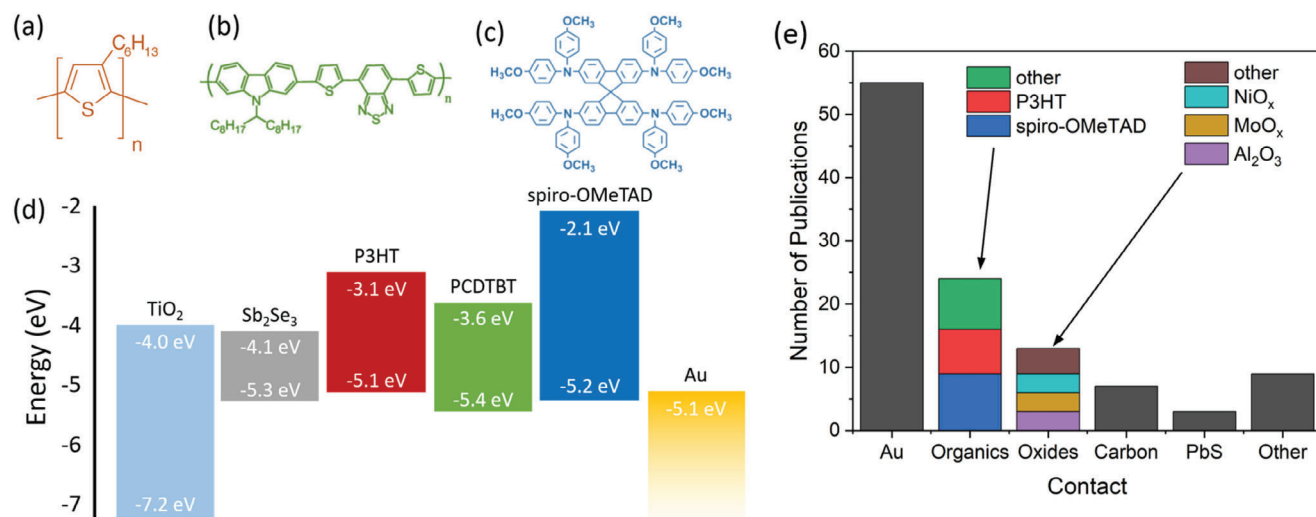


Figure 1. Chemical structure of a) P3HT, b) PCDTBT, and c) spiro-OMeTAD HTM layers used in this work, d) literature values of band positions for each of the layers within the complete solar cell,^[17–21] and e) relative frequency of different back contact structures for superstrate Sb₂Se₃ devices in literature.

technologies, in particular for perovskite solar cells, and therefore is well understood by many research groups who are familiar with the processing route and have optimized recipes. The inclusion of additives to control morphology and molecular dopants results in a high mobility spiro-OMeTAD layer which is used in all record efficiency Sb₂X₃ device structures^[7,8,10] and particularly those with efficiencies above 10%, and therefore is often the default choice for high-efficiency devices. P3HT is commonly used in organic solar cells, and has shown to be effective at blocking pinholes in CdTe devices.^[14] It has also been shown to be an effective HTM for Sb₂Se₃ devices, with efficiencies >6% observed.^[15] There are far fewer reports of Sb₂Se₃ devices incorporating a PCDTBT hole transport layer, however despite this it has also shown to produce high-efficiency devices.^[16] Together, these three organic hole transport layers offer a suitable platform to compare organic hole transport materials in Sb₂Se₃ solar cells to elucidate the role of organic HTMs, establish what attributes are required for effective hole transport, and determine whether spiro-OMeTAD is truly necessary in high-efficiency Sb₂Se₃ devices.

Whilst often unmentioned in literature, the 1D nature of the Sb₂Se₃ unit cell makes film morphology particularly sensitive to deposition conditions. This is especially true for films grown via high-temperature PVD which tend to have large grain sizes and favorable grain orientations, but for which uniform coverage of Sb₂Se₃ has proven challenging. Deposition of a thin, small grain seed layer has been key to improving coverage on the microscale.^[16] Despite this, even minor alterations to absorber layer processing or surface chemistry of the substrate can alter the early-stage nucleation conditions,^[15] which has a drastic impact on film morphology. Such sensitivity to processing conditions can severely hinder device optimization efforts, with each changed variable requiring re-optimization of the Sb₂Se₃ deposition conditions to prevent pinholes. Alternatively, pinhole blocking layers can be used to prevent direct contact between the metal and window layer in areas of poor substrate coverage which would otherwise short-circuit the cell,

thereby improving uniformity drastically.^[14,16] Therefore, these three organic HTMs are also assessed in terms of their pinhole-blocking ability, which is a particularly important aspect for novel absorbers such as Sb₂Se₃ in the early stages of their development.

This study aims to determine what purpose HTM layers serve in Sb₂Se₃ solar cells in two ways. Initially, we use photoemission to study the simple Sb₂Se₃-Au interface in isolation to determine its energy level alignment with reference to its suitability for hole extraction. We then comprehensively study the impact of several organic HTMs against one another in comparable device structures to i) assess the relative efficacy of each, with particular reference to spiro-OMeTAD as the “standard” HTM of choice, ii) compare devices with an organic HTM to those without to better understand the mechanism by which HTMs improve charge extraction, and iii) determine what attributes are necessary for a high-performance HTM in Sb₂Se₃ solar cells. Literature reports of Sb₂Se₃ solar cells typically either use a particular HTM incidentally, whereby the focus is on other aspects of device performance, or report optimization of a single HTM without detailed comparison. Whilst several other organic HTMs have been reported aside from those mentioned here, they tend to be used in lower efficiency (<6%) devices^[22] or are not commercially available.^[23] Given the markedly different device structures and processing routes between different research groups, it is impossible to meaningfully compare the effectiveness of one organic HTM to another from literature alone. Therefore, in this study we initially optimize the deposition conditions for P3HT, PCDTBT and spiro-OMeTAD HTMs. We are then able to directly compare the effectiveness of the three organic HTMs against each other, and also to a reference device without any organic HTM. We find that P3HT produces the highest efficiency devices, although there is a relatively small difference between them and all three HTMs offer comparable device performance. The presence of the organic HTMs result in the absence of rollover in the forward bias region of JV curves, which is typically associated with a back contact barrier. There is no correlation of

device performance with the reported natural band positions of the organic semiconductors which might be expected to determine the effectiveness of hole extraction. The inclusion of a HTM leads to an improvement in all performance parameters, in terms of champion cells and averages compared to Au-only contacts. There is also a drastic reduction on the spread of performance, which is attributed to pinhole blocking by the organic layers preventing short-circuiting through areas with a weak diode response.

2. Results and Discussion

2.1. Energy Level Alignment at the Back Contact of Sb_2Se_3 Devices

P3HT, PCDTBT and spiro-OMeTAD have already been reported in Sb_2Se_3 devices with over 6% power conversion efficiency,^[7,15,16] demonstrating their effectiveness as HTMs. However, the key properties required of a material in order to be an effective HTM in Sb_2Se_3 solar cells remains unclear. An obvious design strategy would be to match the HOMO position of the HTM as closely as possible to the valence band, whilst the LUMO position would be higher than the conduction band minimum of Sb_2Se_3 . This would be expected to facilitate hole extraction whilst repelling electrons, thereby creating a selective contact and minimizing recombination of photo-generated carriers.

Figure 1 shows the chemical structure of each HTM, as well as the equilibrium band positions of the different layers in a complete device structure and a survey of the contact structures used in superstrate devices from literature. We can see from Figure 1e that an Au layer deposited directly onto the back surface of Sb_2Se_3 is the most commonly employed back contact structure in literature, with a range of organic interlayers (typically either spiro-OMeTAD or P3HT) being regularly used as a HTM. We therefore compare the simple Au contact to P3HT and spiro-OMeTAD, as well as to PCDTBT which is comparatively unexplored in Sb_2Se_3 devices.^[16] The range of HOMO positions of the different organic HTM layers studied here (−5.1 to −5.45 eV) encompasses both the VBM of Sb_2Se_3 (−5.26 eV), as well as the work function of Au (−5.1 eV). Therefore, there will be a positive or negative step in the ionisation potential toward the back contact depending on the particular organic HTM used. Similarly, the LUMO positions of the HTMs range from −2.1 to −3.6 eV, compared to the Sb_2Se_3 CBM of −4.1 eV. This implies that all three HTM layers should provide a barrier to electrons in the Sb_2Se_3 conduction band moving toward the back contact, with the barrier height ranging from 0.5 to 2.0 eV, which may reduce electron–hole recombination. Aside from being typical *p*-type transport layers for solar cells, the three HTMs studied here share little commonalities with one another in terms of their structure or electronic properties. Therefore, together they encompass a wide range of properties, from which any material parameters crucial to the effectiveness of a HTM for Sb_2Se_3 devices might be inferred. We note that the energy level alignments shown in Figure 1d, which are based upon the assumption of common vacuum levels, rarely correspond to experimental observations of semiconductor–metal,^[24] semiconductor–organic^[25] nor organic–metal^[26] interfaces in practice, but they provide a rea-

sonable first approximation to the band structure at the back contact of Sb_2Se_3 devices.

From the relative bulk band positions shown in Figure 1d, it would seem that a simple Au contact should enable efficient hole extraction due to its deep-lying work function close to the valence band maximum of Sb_2Se_3 , and the need for additional interlayers such as the organic HTMs is not immediately obvious. From simply comparing the literature values of the bulk valence band and work function of the separate materials, we would expect an offset of ≈ 160 meV between Au and Sb_2Se_3 which would not be expected to pose a significant barrier to hole transport from the absorber to the electrode.^[27] However, predicting the band alignment between two materials brought into contact with one another using measurements of bulk material properties independently is notoriously challenging, and often cannot be reconciled with experimental data.^[17] Therefore, instead we use the Kraut method^[28] to directly study the interface formed between Sb_2Se_3 and Au in order to determine a more reliable estimate of the offset and to better understand the apparent requirement of HTMs, as shown in Figure 2.

The Kraut method is a photoemission-based technique whereby two materials (material A and material B) are measured independently, and the core level to valence band edge ($E_{CL} - E_{VB}$) separation is determined in each case. A third sample is then studied whereby material A is deposited onto material B to form the interface, yet is thin enough that characteristic photoelectrons can escape and be measured to determine the core level separation for the interface sample (ΔCL). The core level shift upon interface formation is directly related to the shift in the valence and conduction bands, and therefore the valence band offset at an interface can be measured as:

$$\Delta E_{VB} = (E_{CL}^B - E_{VB}^B) - (E_{CL}^A - E_{VB}^A) + \Delta E_{CL} \quad (1)$$

This method has previously been used to study the band offsets at the front contact of Sb_2Se_3 solar cells^[17] as well as the band alignment to its native oxide,^[29] and is typically used to determine the valence band offset between two materials. Since it relies on the measurement of core levels from both layers in a heterostructure concurrently, rather than one after another, this method is particularly suited for investigating band alignments and offers a direct measurement of an interface of interest. This is then combined with the core level to valence band separation, which will be constant for a given material and therefore not subject to small shifts with measurement conditions which might otherwise obscure the behavior of interest. Here, we adapt the method slightly to instead measure the offset between the valence band of Sb_2Se_3 and work function of Au.

Figure 2a–c shows the Sb_2Se_3 , Au, and $\text{Sb}_2\text{Se}_3/\text{Au}$ samples respectively that are required for the Kraut analysis, and the survey spectra for each sample is given in Figure 2d–f. These survey spectra are shown here to demonstrate the principle of the Kraut method, however high-resolution scans of the relevant regions were used for subsequent calculations, and can be found in Figure S1 (Supporting Information). The Sb 3d core level is particularly intense, and therefore is monitored during interface formation since this maximizes the chance of being observed through a nominal ≈ 10 nm overlayer of Au. The Sb 3d core level

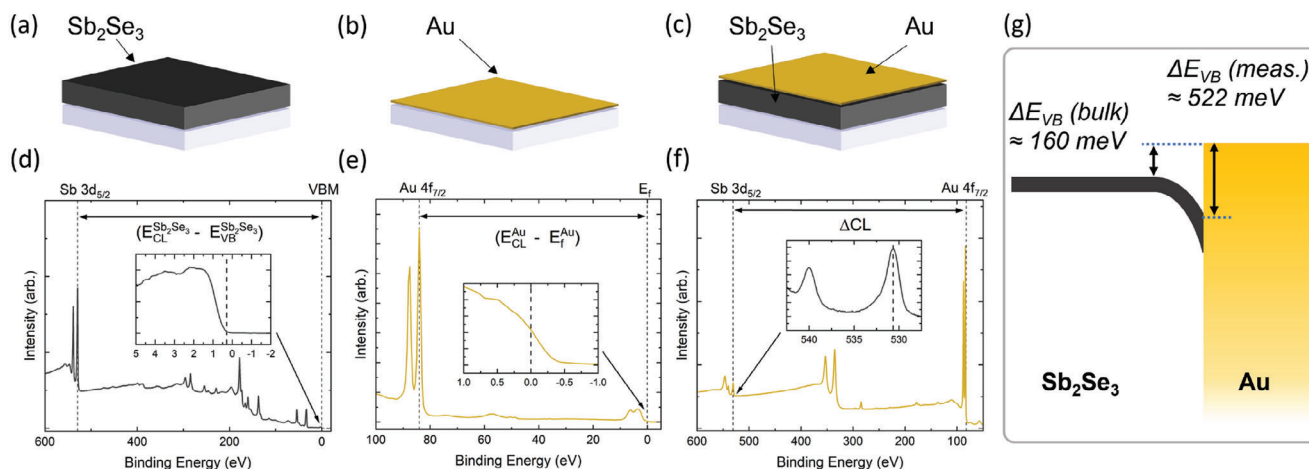


Figure 2. Illustration of the samples fabricated for XPS measurement (a–c), as well as their corresponding survey scans (d–f) required for Kraut analysis. g) shows a comparison of the offset between the valence band maximum of Sb_2Se_3 and the work function of Au by comparing their respective “bulk” band positions ($\Delta E_{\text{VB}}(\text{bulk})$) versus the measured offset using the Kraut method ($\Delta E_{\text{VB}}(\text{meas.})$).

to valence band separation ($E_{\text{CL}}^{\text{Sb}_2\text{Se}_3} - E_{\text{VB}}^{\text{Sb}_2\text{Se}_3}$) is measured for the Sb_2Se_3 sample, the Au 4f to Fermi level ($E_{\text{CL}}^{\text{Au}} - E_{\text{F}}^{\text{Au}}$) is measured for the Au sample, and the core level separation $\Delta\text{CL} = (E_{\text{CL}}^{\text{Sb}_2\text{Se}_3} - E_{\text{CL}}^{\text{Au}})$ is measured for the interface sample. This results in an offset between the valence band maximum of Sb_2Se_3 and work function of Au as 522 meV, which is significantly higher than the 160 meV offset predicted from comparing the separate bulk materials. Despite this large offset between Sb_2Se_3 and Au measured using the Kraut method, the bands must presumably return to their respective bulk values of VBM and work function away from the interface, which would produce downward band bending that is distinct from that expected upon simple alignment of Fermi levels. This is shown in Figure 2g, which does not account for “normal” Schottky barrier formation whereby band bending occurs as a result of charge transfer from one material due to alignment of Fermi levels. The relative band positions at the interface between Sb_2Se_3 and Au may be fixed by Fermi level pinning,^[24] and therefore some degree of downward band bending is expected in the Sb_2Se_3 layer, which could inhibit hole transport despite the seemingly favorable relative bulk band positions of the two materials.

The band alignment shown in Figure 2 indicates the interface between Sb_2Se_3 and Au is highly defective, and may offer some insight as to why Sb_2Se_3 devices (in particular those with high efficiencies) typically incorporate a HTM between the absorber layer and back contact. The additional interlayer would then prevent direct contact between Sb_2Se_3 and Au, which in turn might prevent Fermi-level pinning at the back contact. Ideally, we would assess each of the organic HTMs shown in Figure 1 (i.e., P3HT, PCDTBT and spiro-OMeTAD) by repeating this Kraut method for the different contact structures to make a direct comparison of the offset at the back contact. However the technique requires precise control of the overlayer thickness which is not afforded by spin-coating deposition employed here. Instead, we compare the performance of the organic HTMs against one another, as well as to a simple Au only contact, using a device-led approach detailed below.

2.2. Device Optimisation and Performance

Previous reports of the inclusion of P3HT, PCDTBT, and spiro-OMeTAD in Sb_2Se_3 solar cells have already demonstrated their potential as effective HTM layers in high-efficiency devices. However, different processing steps and baseline device performance of different research groups do not allow for a meaningful comparison of the effectiveness of organic HTMs from literature alone. Therefore before making a detailed assessment of their relative efficacy, each organic layer underwent an extensive optimization process to ensure a fair comparison between device structures. The main findings of this are briefly reported below, and is shown in further detail within the Supporting Information. Figure 3 summarizes the results of the optimization process, with box plots showing the efficiency of devices as a function of spin coating speed and solution concentration for each organic HTM. We note that the device optimization process for each of the different organic HTMs was not undertaken concurrently, therefore gradual changes in the CSS source condition can lead to varied baseline device efficiency. For this reason, we defer the comparison between HTMs to the discussion of Figure 4.

Devices with a P3HT layer at the back contact show a strong dependence on solution concentration, with a gradual improvement in both the peak and average efficiency for most spin speeds shown in Figure 3a. This is a result of a drastic improvement in all performance parameters (see Figure S2, Supporting Information) with higher P3HT solution concentration, which are expected to produce increasingly thicker P3HT films. The improved average efficiency is a result of a much more uniform performance across the device plate for thicker P3HT films. Therefore, 10 mg mL⁻¹ P3HT solutions in chlorobenzene were found to be optimal for both peak and average device performance, and is used in all P3HT devices described hereafter. There was no further improvement observed when the solution concentration was increased beyond 10 mg mL⁻¹.

Devices with a PCDTBT layer show improved average efficiency for solution concentrations up to 5 mg mL⁻¹, due to improvements to the V_{oc} and shunt resistance (see Figure S3,

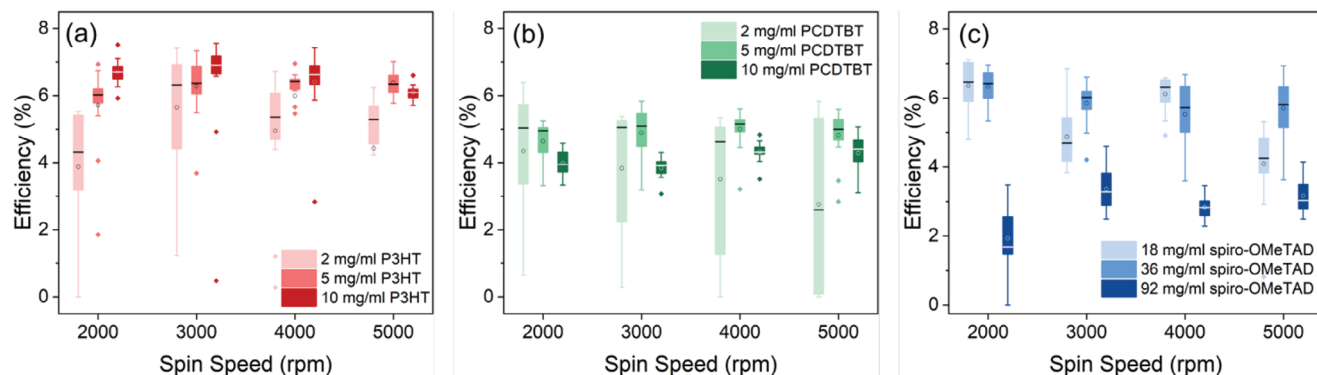


Figure 3. Box plots showing efficiency of Sb_2Se_3 solar cells with a) P3HT, b) PCDTBT, and c) spiro-OMeTAD layers spin-coated onto the back surface prior to metallization. The solution concentration in chlorobenzene and spin speed during deposition were varied in tandem for each device structure ($N = 16$).

Supporting Information), as well as more uniform performance across the device plate. Beyond this, performance is gradually lowered due to an increase in series resistance thereby lowering the fill factor. Therefore, Figure 3b demonstrates the two competing effects of PCDTBT - the pinhole blocking effect (discussed in more detail below) reduces the spread in performance across a device, but introduces an additional layer whose presence increases the series resistance. With this in mind, 5 mg mL^{-1} solutions of PCDTBT were determined to produce the optimal balance between improving performance whilst introducing minimal additional series re-

sistance, and therefore is used in the subsequent PCDTBT devices.

Devices with a spiro-OMeTAD layer, shown in Figure 3c, were optimized using significantly higher solution concentrations compared to P3HT and PCDTBT, as is typical for such HTM layers used in literature.^[30] It is also noted that the spiro-OMeTAD layers require additional dopants to improve the hole mobility (hence the Li-TFSI and tBP additives used here), which is a slow, gradual process.^[31] This is demonstrated in Figure S5 (Supporting Information), whereby the efficiency of devices improves over time as the series resistance is lowered, with the rate

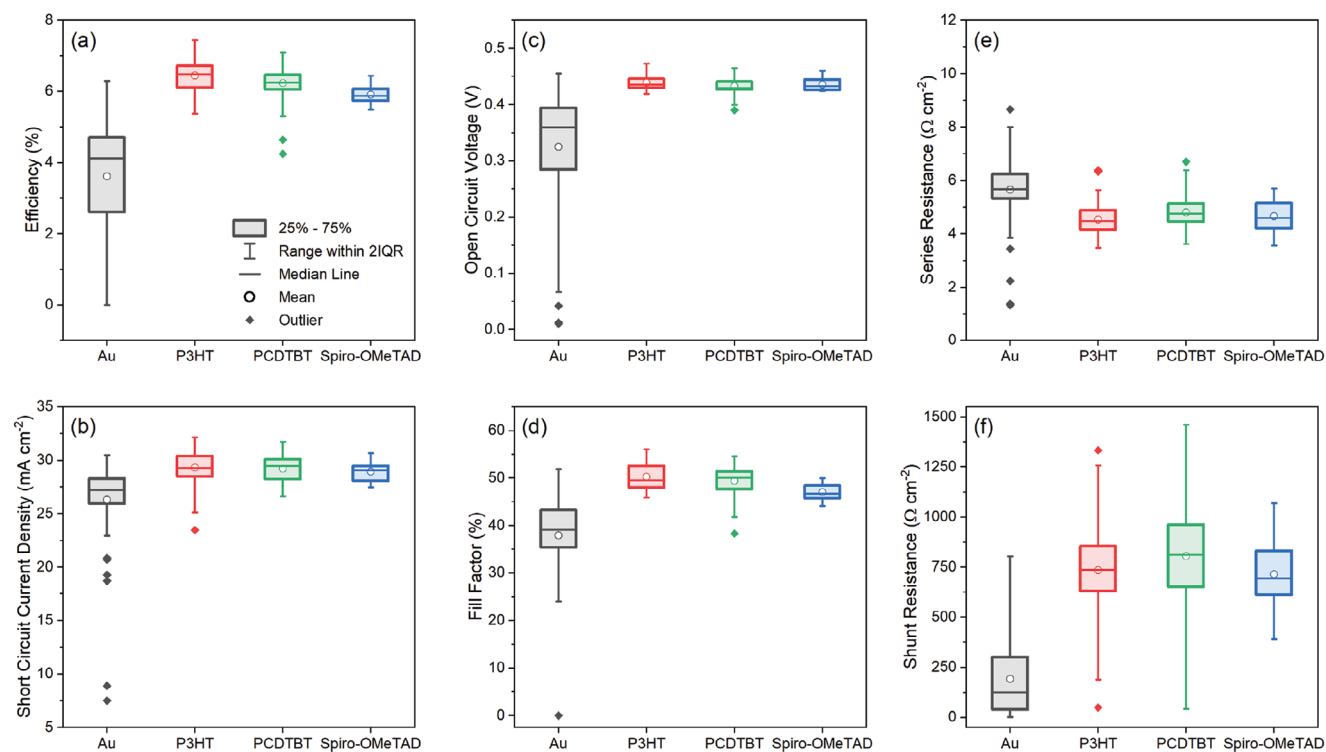


Figure 4. Box plots showing the performance parameters for devices with an Au-only contact compared to those including optimized P3HT, PCDTBT or spiro-OMeTAD HTM layers. The a) efficiency, b) J_{sc} , c) V_{oc} , d) fill factor, e) series resistance and f) shunt resistance is shown for each device structure ($N = 64$).

and extent of improvement dependent on spiro-OMeTAD solution concentration and therefore also on the thickness of the resultant layer. For this reason, devices were left in air for at least 3 days before comparing them. Despite this, spiro-OMeTAD layers were noted to exhibit a degree of variability in their resistivity which hindered optimization efforts somewhat, and maybe result of the more complex solution preparation and doping process compared to the other organic layers.^[32] We note that strict control of the environmental conditions under which the devices were left to oxidize did not have a substantial effect on the reproducibility of device performance (Figure S6, Supporting Information). Figure 3c shows that devices with 18 and 36 mg mL⁻¹ spiro-OMeTAD layers perform similarly well, whereas 96 mg mL⁻¹ solutions results in much lower efficiencies. This is due to a large increase in series resistance lowering overall performance, as shown in Figure S4 (Supporting Information), although despite this, the open circuit voltage continues to improve with higher solution concentrations. With little consistent differences for devices using lower solution concentrations, subsequent spiro-OMeTAD layers are deposited from 36 mg mL⁻¹ solutions as this matches closely with similar processing routes used in the current record efficiency Sb₂Se₃ device.^[7]

It is noted that for each organic HTM, the spin speed with which they are processed has a relatively minor effect on device performance. The thickness of the spin-coated layer is expected to be roughly proportional to the inverse of the square root of spin speed, and therefore is expected to have a significant effect on device performance. Instead, the solution concentration is found to have the dominant effect. This may be a result of the rough Sb₂Se₃ surface on which the HTMs are deposited, which could affect the film formation. However, the observation of similar trends in the performance of device with different solution concentrations for each spin speed increases confidence in results, and instead act largely as repeat measurements. Therefore, 3000rpm was chosen somewhat arbitrarily as the optimal spin speed, and is kept consistent for each HTM in subsequent depositions.

Further sample sets were fabricated to investigate the effect of several other processing variables during the optimization procedure, however there were no notable improvements observed. For example, whereas post deposition annealing of CdTe devices with organic HTMs has proved to be a key processing step, improving the crystallinity of P3HT^[14] and accelerating the slow doping process in spiro-OMeTAD,^[33] it was found to be detrimental for all devices studied here. As shown in Figure S7 (Supporting Information), annealing Sb₂Se₃ devices following the deposition of an organic HTM appears to have a pronounced negative effect on device performance. Considering a similar reduction in efficiency is also observed in devices without any organic HTM, we consider this efficiency reduction with annealing to be due to deterioration of the Sb₂Se₃ itself, rather than the organic HTMs.

Having found the optimal processing conditions for each organic HTM, a series of devices were then fabricated to directly compare the effect of P3HT, PCDTBT and spiro-OMeTAD HTM layers, compared to a simple Au contact. A total of 16 devices were fabricated from consecutive Sb₂Se₃ depositions in a randomized order (thereby minimizing the effect of gradual drift in CSS conditions), with each device containing 16 individual cells (i.e., 64

cells for each device structure). This allows a direct comparison of the effect of the organic HTMs on device performance across a large sample set, with box plots showing the JV performance parameters shown in Figure 4.

The addition of an organic HTM layer at the back contact of Sb₂Se₃ compared to a simple Au contact leads to a dramatic improvement in both the average device performance, as well as increasing the maximum attainable efficiency, as discussed in Section 2.3. The average efficiency is improved from (3.6 ± 1.6)% for a simple Au contact, to (6.4 ± 0.4)%, (6.2 ± 0.4)% and (5.9 ± 0.3)% for P3HT, PCDTBT, and spiro-OMeTAD contacts respectively. This is accompanied by a much narrower distribution of all performance parameters for devices with an organic HTM, irrespective of which particular HTM is used. The improvement in average device performance is attributed to a pinhole-blocking effect, which is discussed in more detail in Section 2.4. Whilst the average and champion efficiency of P3HT devices is marginally higher than for PCDTBT, the differences are small and not statistically significant following one-way ANOVA analysis ($p = 0.05$). The difference between P3HT and spiro-OMeTAD devices, whilst still relatively small, is slightly more pronounced. The difference arises from a reduction in fill factor, despite similar series and shunt resistances. Comparison of individual JV curves (an example of each is given later in Figure 5a), indicates a lower ideality factor may be responsible for the reduced performance of devices with a spiro-OMeTAD layer. Whilst this could occur for any number of reasons, one possibility is the diffusion of Li into the Sb₂Se₃ layer from the Li-TFSI additive, which is expected to occur quickly due to the small ion size. This would compensate for any native doping of the Sb₂Se₃ as indicated by a comparatively low doping density as shown in Figure S8 (Supporting Information), which also results in a narrower space charge region compared to the other devices. Aside from this, all other performance parameters are improved with the addition of any of the organic HTMs tested here to the same extent, with no statistically significant differences between them. We do however note that the stability of devices over several months is strongly dependent on the back contact structure. Whilst most devices were found to be remarkably stable, devices containing a P3HT layer were particularly prone to degradation, with a 40% reduction in efficiency observed over a 10 week period (Figure S9, Supporting Information). This relatively quick degradation in an otherwise stable device structure is likely due to photo-oxidation of the P3HT layer.^[34,35] We find that the molecular weight of the P3HT has no clear impact on the degradation rate, however alternative mitigation strategies could include device encapsulation or stabilizing additives if necessary.

As well as improved average performance, the efficiency of the best performing cells is significantly improved for device structures that include an organic layer, which again is a result of improvement in all performance parameters, which can be seen from Table 1. We note that this improved champion efficiency is not simply due to a reduction in shunted areas, which improves the average efficiency. Instead, the series resistance of devices with an organic HTM is lower than the control device without, despite the inclusion of an additional layer with intrinsic resistivity, and increasing the number of interfaces in the device stack. Although the control (Au) device does have several cells with particularly low (<4 Ω cm²) series resistance, these are poorly rectifying and therefore this a result of a short-circuit rather than

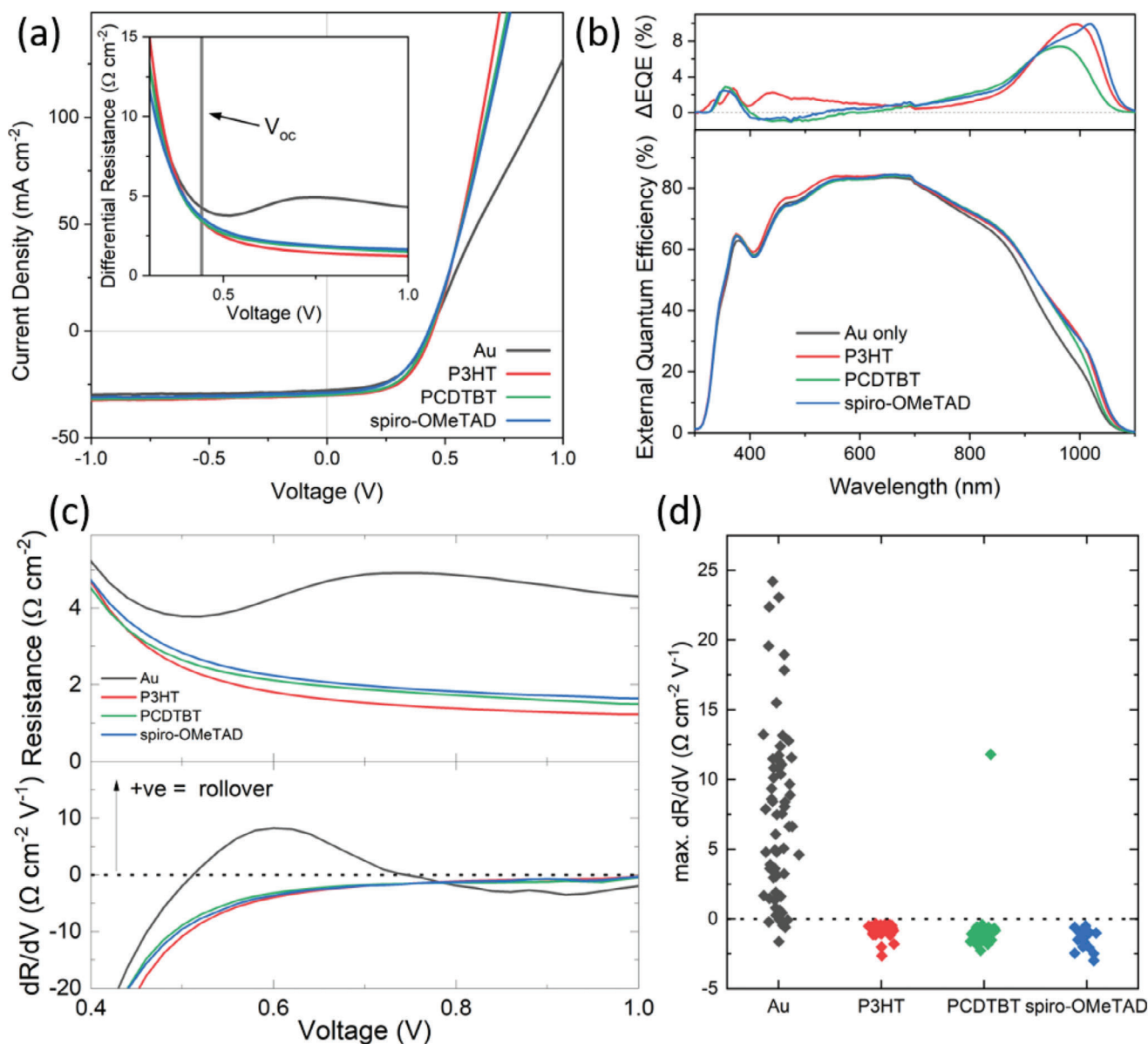


Figure 5. a) JV curves of champion cells from devices with Au-only contacts compared to those with P3HT, PCDTBT and spiro-OMeTAD HTM layers between the Sb_2Se_3 and Au. Inset is the differential resistance calculated at each point along the JV curves, with the forward bias region shown in detail. The range of V_{oc} found for these devices is also marked to indicate the region where series resistance is calculated from. b) External quantum efficiency (EQE) of the same devices. The difference between EQE response of devices with an organic HTM layer compared to the Au-only device is also shown (ΔEQE) as a function of wavelength. c) Differential resistance plot shown in (a) as well as its derivative, which is used as a qualitative indicator of rollover in JV curves when $dR/dV > 0$, and d) maxima of dR/dV plots for each HTM structure for all contacts measured.

a truly lower series resistance in the device. The mechanism by which the organic layers improve the champion device efficiency is explored in more detail in Section 2.3.

2.3. Rollover and Schottky Barriers

JV curves of the highest efficiency contact for each device structure are shown in Figure 5a. The differential resistance plot is shown inset, highlighting the forward bias region such that subtle variations in the series resistance between device structures

can be more clearly seen. All curves look very similar below V_{oc} , with differences in performance being due to an improvement in the fill factor and J_{sc} for devices with an organic HTM compared to an Au only contact. In forward bias, differences become more apparent. The device without an organic HTM (i.e., Au) displays a gradual current limiting effect above V_{oc} whereby the JV curve starts to flatten. This “rollover” phenomenon is observed across a wide range of solar cell architectures^[27] and is characteristic of a Schottky barrier and the back contact between the Sb_2Se_3 and Au layers. The observation of rollover in JV curves with an Sb_2Se_3 -Au contact despite a seemingly favorable alignment of bulk band

Table 1. Performance parameters of the highest efficiency contacts for devices with different back contact structures.

Contact	η (%)	V_{oc} (V)	J_{sc} (mA cm ⁻²)	FF (%)	R_s (Ω cm ²)	R_{sh} (Ω cm ²)
Au	6.29	0.437	27.7	51.9	4.62	803
P3HT	7.44	0.445	30.1	55.4	3.67	583
PCDTBT	7.09	0.437	29.9	54.2	3.70	616
spiro-OMeTAD	6.40	0.430	28.9	51.5	3.89	622

positions (Figure 5), as well as an anomalously large measured band offset (Figure 2) implies deviation from the behavior expected from the Schottky–Mott rule, which is likely a result of Fermi-level pinning. This Schottky barrier acts in the opposite direction to the main junction and therefore inhibits current flow in forward bias. The presence of a back contact barrier leads to a reduction of the fill factor, and in extreme cases whereby the main junction and back contact barrier overlap, a reduction in V_{oc} is also observed.^[36] The extent of the rollover effect for Au devices in Figure 5a may be seen more clearly by taking the differential resistance, whereby the inverse of the gradient is calculated at each point along the JV curve. This is shown inset, and the resistance decreases up to V_{oc} for the Au-only device, before rising again at further forward bias.

Devices with an organic HTM do not show such rollover effect in any of the JV curves, and the differential resistance decreases for each with increasing forward bias until a plateau is reached. This implies the Schottky barrier at the back contact has either been eliminated or reduced to the point where it no longer significantly affects charge transport out of the device. The improved charge extraction is then directly related to the increase in fill factor and J_{sc} for devices with an organic HTM. This is supported by external quantum efficiency measurements, shown in Figure 5b, where there is an increase in current collection at long wavelengths for devices with an organic HTM. Since longer wavelength photons will penetrate deeper into the absorber layer, carriers are more likely to be photogenerated close to the back contact. In particular, according to Chen et al.,^[37] photons with wavelength ≈ 1000 nm will penetrate $\approx 1 \mu\text{m}$ into the Sb_2Se_3 absorber, which is close to the average thickness of Sb_2Se_3 in our devices. We would expect a decrease in collection efficiency for carriers which are photogenerated close to the Sb_2Se_3 -Au interface, which if defective will swiftly result in recombination. Therefore the increase in long wavelength collection in this region with organic HTMs is likely related to the lowering of the Schottky barrier between Au and Sb_2Se_3 allowing efficient charge extraction due to a better passivated interface. Similar effects have been seen for CdTe-based solar cells using organic contact layers.^[14]

Given the implied differences in the Schottky barrier at the back contact for the devices studied here, we have attempted to extract quantitative values of the barrier height using temperature-dependent dark JV measurements as outlined by Batzner et al.^[38] However, as of yet this has not been possible due to observation of slow transient current effects producing inconsistent series resistance measurements (in dark only, light JV curves reported above are unaffected), rendering this method of barrier height measurements unreliable. The cause of this effect remains unclear and is under study at present. Instead, we use

the extent of rollover observed in individual JV curves to give a qualitative assessment of the barrier height in our devices. Given that rollover is indicated by a flattening of the JV curve in forward bias, which corresponds to an increase in the differential resistance, the gradient of the differential resistance can be used as an indicator of the degree of rollover and therefore barrier height. Where the differential resistance increases, this can be identified as a positive dR/dV , as shown in Figure 5c. Here we see that the device with a Au-only contact has a positive dR/dV between $\approx 0.5 - 0.7$ V, whereas the devices with an organic HTM always have $dR/dV < 0$ (the PCDTBT data point which implies rollover is the result of a discontinuity in the JV curve resulting from a measurement artefact). This simple method of qualitative barrier height determination can be easily applied to large number of JV curves, and the maxima of the dR/dV curve can therefore be used as an indicator of the presence, and relative extent, of contact barriers. This is especially useful in instances where the presence of rollover is not immediately obvious, with a subtle flattening of JV curves in forward bias. By applying this method to all of the devices shown in Figure 4 (corresponding to over 250 individual cells), we see that rollover is consistently observed across devices with an Au-only contact, but not with organic HTMs. We note that many of the contacts with a low max. dR/dV for the Au contact will be those which were poorly rectified due to the presence of pinholes, and therefore in this case would not be expected to show any rollover due to their linear JV curves.

We can therefore conclude with some confidence that there is a Schottky barrier formed between Sb_2Se_3 and Au when deposited directly onto the back surface, yet the addition of an organic interlayer prevents barrier formation. The reduction/removal of the barrier does not appear to be strongly dependent on which specific organic is used, and given the wide range of both organic and inorganic HTM layers found in literature,^[13] the dominant effect maybe to simply separate the Sb_2Se_3 and Au layers and prevent a defective interface forming directly between these two materials. If this is the case, then separating direct contact between Sb_2Se_3 and Au, for example with an organic interlayer, prevents this unfavorable interface forming by electrostatically decoupling the two layers,^[39] which then prevents the formation of a Schottky barrier which can impede hole extraction. This would explain the relative insensitivity of Schottky barrier formation to the specific organic HTM used in this study, as well as why such a wide range of other HTMs are found in the literature to work equally well,^[13] including the native oxide.^[40] A similar strategy of “contact displacement,” whereby a particularly thin interlayer is placed between the absorber and charge extraction layer in order to limit non-radiative recombination at a defective interface, has been explored in perovskite literature.^[41] Dielectric interlayers deposited at metal-organic semiconductor interfaces have also been demonstrated to reduce the charge injection barrier by depinning the Fermi-level.^[42]

According to this interpretation, a wide range of materials, both organic and inorganic, will function as effective HTMs in a Sb_2Se_3 device structure. Poly[bis(4-phenyl)(2,4,6-trimethylphenyl)amine] (PTAA) is another common organic HTM which has shown promise in other PV technologies, in particular for perovskites, yet has scarcely been employed in Sb_2Se_3 devices to date. As shown in Figure S10 (Supporting Information), with minimal process optimization the PTAA appears to

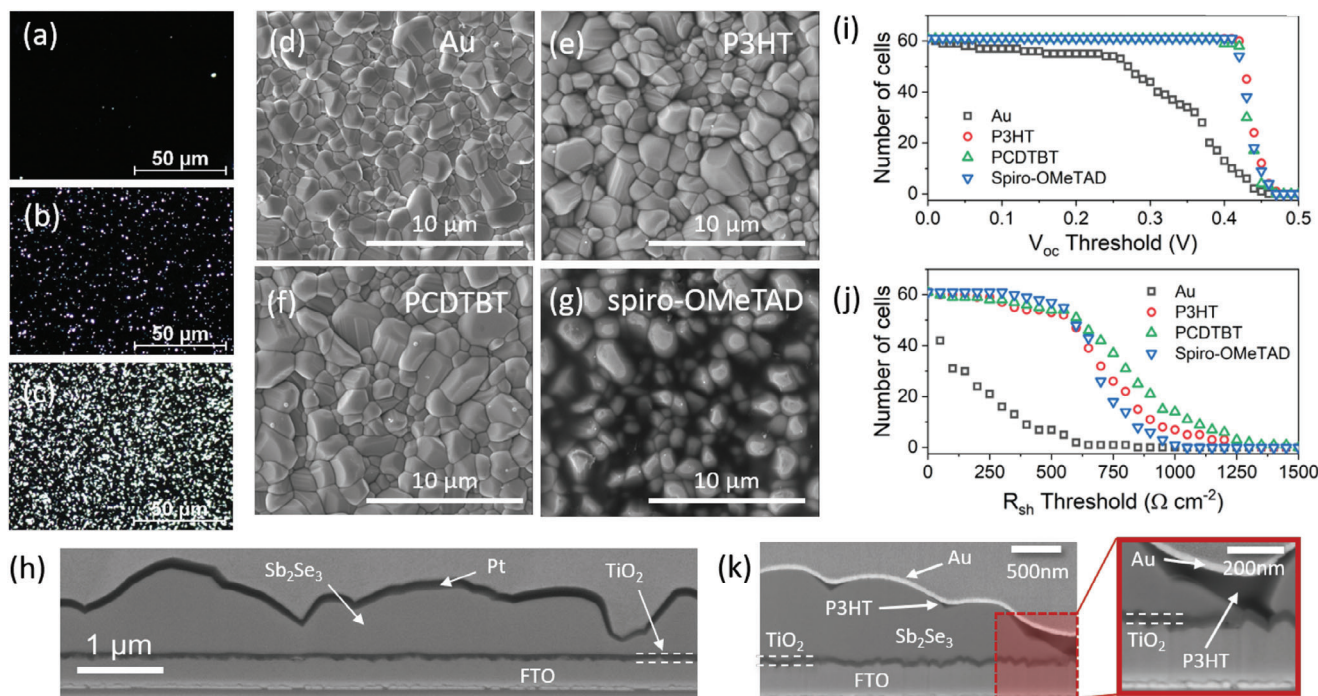


Figure 6. a–c) Backlit optical microscope images of Sb_2Se_3 films using progressively higher substrate temperatures during the seed layer deposition, resulting in a gradual increase in the number of bright spots, which correspond to incomplete coverage of the absorber layer. d–g) SEM images of the back surface of Sb_2Se_3 coated with different organic HTM layers. h, k) cross section of Sb_2Se_3 device showing non-uniform thickness of the absorber layer and demonstrating how P3HT can accumulate at the thinner regions, preventing contact between the front and back electrodes. i, j) shows the number of contacts whereby the performance parameter is greater than an arbitrary, moving threshold for different back contact structures.

function in much the same way as the other organic HTMs tested so far. In particular, the rollover in the forward bias of JV curves is eliminated for all devices with a PTAA interlayer, further suggesting the dominant role of the HTM is to separate a defective Sb_2Se_3 -Au interface and prevent Schottky barrier formation. The device efficiency is then determined by balancing the need for a lower Schottky barrier without introducing excessive series resistance from the HTM itself, although we note that further optimization through extrinsic doping of the PTAA layer may yield further benefits. Given the relative insensitivity to specific HTMs found in this work, the eventual removal of all organic layers and replacement with inorganic HTMs (for example metal oxides) may offer a promising route to improve the stability of Sb_2Se_3 devices in the long term if they are to move beyond lab-scale. Despite this apparent insensitivity, we expect that typical HTM considerations such as a well-matched valence band offset and minimal additional series resistance, will remain vital. In this respect, detailed transport measurements to correlate charge extraction efficacy with different contact structures more closely would be of great benefit.

2.4. Pinhole Blocking

As observed in Figure 4, the presence of the organic HTM layers improves not only the champion efficiency, but the average performance across a device plate also increases drastically. Whereas it may be possible to reduce such spread of device performance

with a simple Au contact though careful process control, a simple and effective method of ensuring narrow performance distributions is crucial for lab-scale studies of solar absorbers, especially for technologies at an early stage in their development. **Figure 6a–c** shows back-lit optical microscope images of a several Sb_2Se_3 thin films with varying degrees of substrate coverage as demonstrated by bright spots, which correspond to areas of exposed transparent substrate which are not covered by highly absorbing Sb_2Se_3 . Such poor substrate coverage is easily obtained outside of the Sb_2Se_3 optimal CSS processing conditions, with the examples given corresponding to growth runs where the seed layer is deposited at slightly higher than optimal substrate temperatures. The peculiar, 1D grain structure of Sb_2Se_3 means that it is particularly challenging to control the morphology of vapor deposited films to ensure uniform coverage,^[16] often resulting in highly non-uniform absorber thickness (as shown in Figure 6h), and therefore pinholes can easily form. Pinholes provide alternative routes for current to bypass the main junction of the solar cell and in drastic cases, such as those shown in Figure 6c, this would typically result in a non-rectifying cell due to direct contact between the Au back electrode and the front of the device stack. However, we have found that the use of any of the organic HTMs tested here in such devices has resulted in reasonable (>5%) performance, even in the case of films with extremely poor Sb_2Se_3 coverage. Therefore, whilst pinholes would ideally be avoided entirely, they can be effectively mitigated via the use of an organic pinhole-blocking HTM. The use of solution deposition for the organic layers is important, since this allows the organic to

preferentially accumulate at regions of thin Sb_2Se_3 , which are at most risk of pinholes. This can be observed in Figure 6d–g, and most clearly in the case of spiro-OMeTAD which has a much thicker organic layer due to deposition from a higher solution concentration.

To further highlight the role organic HTMs play in blocking pinholes, thereby “fixing” otherwise poor performing cells and increasing average efficiencies, Figures 6(i, j) show the number of cells with performance parameters which are greater than an arbitrarily set, moveable threshold level. As this threshold is gradually increased, fewer and fewer contacts meet this criteria, therefore the number of “working” contacts decreases. The V_{oc} and R_{sh} have been shown here since they are expected to be most sensitive to pinholes and shunting, however the other device parameters follow similar trends. In both cases, devices with an Au contact have some contacts which work reasonably well. However, this represents only a small fraction of the total number of cells, and the majority perform poorly (i.e., $V_{oc} < 400$ mV and $R_{sh} < 500 \Omega \text{ cm}^{-2}$). On the other hand, all devices with an organic HTM perform much better, with no evidence of shunted devices in each case. Figure 6k demonstrates how the spin-coated organic layers (in this case P3HT) can accumulate preferentially at grain boundaries due to the spin-coating deposition process. The inset shows an area where the Sb_2Se_3 grains leave an area of the underlying TiO_2 exposed, which would be in contact with the Au in the absence of an organic layer, offering a low resistance shunting pathway for a large amount of current to bypass the solar cell without a strongly rectifying junction. However, the P3HT has accumulated in this region, which increases the resistance by several orders of magnitude in this localized area (see Figure S11, Supporting Information), therefore preventing direct contact between the front and back electrodes which would otherwise short-circuit the solar cell which results in improved average device efficiency through pinhole blocking. Each of the organic HTMs are expected to perform a similar pinhole blocking function given their equally narrow distribution of performance parameters.

3. Conclusion

This work offers an in-depth study into the role of organic HTM layers in Sb_2Se_3 solar cells. After optimizing three different organic HTM layers, these were compared against each other, and against a reference device with a simple Au contact. According to the relative bulk band positions of Sb_2Se_3 and Au, the presence of a Schottky barrier would not be expected from simple Schottky–Mott theory. However, photoemission measurements of the $\text{Sb}_2\text{Se}_3/\text{Au}$ interface suggest a degree of Fermi-level pinning, which is relaxed with the inclusion of the organic layers due to physical separation of the layers and therefore preventing the formation of a defective interface. The use of any of the organic HTM layers improved both the average and champion efficiency of devices significantly, challenging the assumption that spiro-OMeTAD specifically is required for optimal performance. However, the stability of devices over several months shows a strong dependence on the back contact structure, and devices with a P3HT HTM produced the highest efficiency contacts, yet also had the fastest rate of performance degradation. The average performance is improved by a pinhole blocking effect, whereby the solution processed organic layer coats the Sb_2Se_3 back surface non-

uniformly, preferentially segregating to grain boundaries and areas of poor substrate coverage. This prevents short-circuiting of the device, therefore significantly increasing the average device efficiency by suppressing the number of shunted contacts. The champion efficiency of devices with an organic HTM is also improved, by lowering a Schottky barrier which forms between the Sb_2Se_3 back surface and the Au contact and would otherwise inhibit hole extraction. This is indicated by a complete removal of rollover in JV curves when devices are in forward bias. This work demonstrates the relaxed requirements for an effective HTM in Sb_2Se_3 devices, with the dominant mechanism for improved champion device efficiency being to physically separate the defective Sb_2Se_3 -Au interface without introducing excessive additional resistivity.

4. Experimental Section

Device Fabrication: Sb_2Se_3 devices were grown in superstrate configuration on $\text{SnO}_2:\text{F}$ coated soda-lime glass substrates (Tec15, NSG Group). A TiO_2 window layer was deposited by spin coating 250 μL of 0.3M titanium isopropoxide dissolved in ethanol, before annealing for 10 min at 110°C under nitrogen to evaporate the solvent. Once the substrate had cooled, this spin-coating step was repeated to produce a 60 nm TiO_2 film. A further 30 min anneal at 500 °C was carried out in the air to crystallize the film into anatase TiO_2 . Sb_2Se_3 films were grown via close-spaced sublimation in a two step process described previously.^[16] Briefly, a compact seed layer was grown with a substrate temperature of 350 °C for 15 min under vacuum, before deposition of a larger grained layer at $T_{sub} = 480$ °C for a further 15 min at a back-filled pressure of 10 Torr nitrogen, producing an average Sb_2Se_3 thickness of $\approx 1.2 \mu\text{m}$.

Where an organic HTM was included in the device structure, 100 μL of a solution of the organic material in chlorobenzene was dynamically spin coated onto the back surface of the Sb_2Se_3 for 30s at spin speeds between 2000 and 5000 rpm. P3HT (RR = 93.6%) and PCDTBT solutions were made at a concentration of 10 mg mL^{-1} in chlorobenzene, with aliquots diluted to 2 and 5 mg mL^{-1} , corresponding to the typical range of concentrations found for Sb_2Se_3 devices. Spiro-OMeTAD was dissolved at higher solution concentrations, following reports from perovskite literature,^[30] which has inspired the typical processing of the HTM when used for Sb_2Se_3 devices. A 92 mg mL^{-1} solution of spiro-OMeTAD in chlorobenzene was prepared, to which 13 $\mu\text{L mL}^{-1}$ Lithium bis(trifluoromethanesulfonyl)imide (Li-TFSI, from a 520 mg mL^{-1} stock solution in acetonitrile), and 13 $\mu\text{L mL}^{-1}$ 4-*tert*-butylpyridine (tBP) was added. Again, aliquots of this solution were similarly diluted in chlorobenzene to produce 18 and 36 mg mL^{-1} solutions of spiro-OMeTAD for comparison.

After deposition of the organic layers, 50 nm Au was deposited onto the back surface via thermal evaporation through a shadow mask to define 16 separate 0.1 cm^2 contacts on each $2.5 \times 2.5 \text{ cm}^2$ device plate. Regions of each device were mechanically scribed to expose the underlying FTO, which was covered with silver paste to form the front contact.

Characterization Techniques: All current density–voltage (JV) measurements were taken under AM1.5G illumination from a TS Space Systems solar simulator (class AAA) calibrated to 1000 Wm^{-2} using a Si reference diode, and recorded using a Keithley 2400 SMU. External Quantum Efficiency (EQE) measurements were taken using a Bentham PVE300 system at 5nm intervals. Data was recorded both with and without a DC light bias from a halogen lamp in addition to the chopped probe beam, and showed only minor differences between the scans,^[15] therefore scans taken without additional light bias were reported. A JEOL JSM-7001F scanning electron microscope (SEM) was used to image the back surface of films with a typical accelerating voltage of 5 kV in secondary electron mode. Cross section sample preparation was obtained by mounting the devices between two mica slides using Allied Tech Epoxy Bond 110, followed by cross section ion polishing using a Hitachi E-3500 Ion Mill. Imaging of these cross

section was performed using a Carl Zeiss Sigma 300 VP SEM operated at 20keV with a 60 μm aperture at 53 Pa in VP mode, whilst detecting backscattered electrons.

Photoemission measurements were taken using Kratos Supra Axis XPS, using a monochromated Al K α x-ray source, ($h\nu = 1486.6\text{eV}$) operating at 225 W with a pass energy of 40 eV. Core levels were fitted in CasaXPS using a pseudo-Voigt function after subtraction of a Shirley background. The valence band edge of Sb₂Se₃ was determined via linear extrapolation of the onset, and the Fermi edge of Au was fitted with a Gaussian-broadened Fermi–Dirac distribution. Three samples were prepared to implement the Kraut method. First, a thick (1 μm) Sb₂Se₃ layer was deposited onto TiO₂ coated Tec15 glass via CSS as described above. The second sample consisted of 100 nm Au evaporated onto Tec15 glass. Finally, the “interface” sample consisted of a 10 nm Au film thermally evaporated onto a 1 μm Sb₂Se₃. It was noted that the 10 nm Au overlayer thickness was chosen by monitoring the decrease in sheet resistance to ensure sufficient film coverage, however the observation of core levels from the underlying Sb₂Se₃ implies some regions are likely to be thinner than the nominal thickness determined via a QCM due to its morphology.

Supporting Information

Supporting Information is available from the Wiley Online Library or from the author.

Acknowledgements

Funding for the work was provided by EPSRC via EP/W03445X/1. Dr. Mark Isaacs is thanked for the acquisition of x-ray photoemission spectra via HarwellXPS.

Conflict of Interest

The authors declare no conflict of interest.

Data Availability Statement

The data that support the findings of this study are openly available in Zenodo at [10.5281/zenodo.11110437](https://doi.org/10.5281/zenodo.11110437), reference number 11110437.

Keywords

back contact, hole transport, organic, pinhole blocking, Sb₂Se₃, Schottky barrier, uniformity

Received: May 7, 2024

Revised: September 20, 2024

Published online:

- [1] H. El-Shair, A. Ibrahim, E. Abd El-Wahabb, M. Afify, F. Abd El-Salam, *Vacuum* **1991**, 42, 911.
- [2] S. Resalati, T. Okoroafor, A. Maalouf, E. Saucedo, M. Placidi, *Appl. Energy* **2022**, 313, 118888.
- [3] J. Jean, P. R. Brown, in *Emerging Photovoltaic Technologies*, IOP Publishing, Bristol, UK **2020**, pp. 2053–2563.
- [4] C. H. Don, H. Shiel, T. D. C. Hobson, C. N. Savory, J. E. N. Swallow, M. J. Smiles, L. A. H. Jones, T. J. Featherstone, P. K. Thakur, T.-L. Lee, K. Durose, J. D. Major, V. R. Dhanak, D. O. Scanlon, T. D. Veal, *J. Mater. Chem. C* **2020**, 8, 12615.
- [5] A. Zakutayev, C. M. Caskey, A. N. Fioretti, D. S. Ginley, J. Vidal, V. Stevanovic, E. Tea, S. Lany, *J. Phys. Chem. Lett.* **2014**, 5, 1117.
- [6] R. E. Williams, Q. M. Ramasse, K. P. McKenna, L. J. Phillips, P. J. Yates, O. S. Hutter, K. Durose, J. D. Major, B. G. Mendis, *ACS Appl. Mater. Interfaces* **2020**, 12, 21730.
- [7] Y. Zhao, S. Wang, C. Li, B. Che, X. Chen, H. Chen, R. Tang, X. Wang, G. Chen, T. Wang, J. Gong, T. Chen, X. Xiao, J. Li, *Energy Environ. Sci.* **2022**, 15, 5118.
- [8] Y. Zhao, S. Wang, C. Jiang, C. Li, P. Xiao, R. Tang, J. Gong, G. Chen, T. Chen, J. Li, X. Xiao, *Adv. Energy Mater.* **2022**, 12, 2103015.
- [9] Z. Duan, X. Liang, Y. Feng, H. Ma, B. Liang, Y. Wang, S. Luo, S. Wang, R. E. I. Schropp, Y. Mai, Z. Li, *Adv. Mater.* **2022**, 34, 2202969.
- [10] S. Wang, Y. Zhao, B. Che, C. Li, X. Chen, R. Tang, J. Gong, X. Wang, G. Chen, T. Chen, J. Li, X. Xiao, *Adv. Mater.* **2022**, 34, 2206242.
- [11] C. Chen, L. Wang, L. Gao, D. Nam, D. Li, K. Li, Y. Zhao, C. Ge, H. Cheong, H. Liu, H. Song, J. Tang, *ACS Energy Lett.* **2017**, 2, 2125.
- [12] S. Wang, Y. Zhao, L. Yao, C. Li, J. Gong, G. Chen, J. Li, X. Xiao, *Sci. Bull.* **2022**, 67, 263.
- [13] G. Jeong, S. Ji, J. Choi, J. Jung, B. Shin, *Faraday Discuss.* **2022**, 239, 263.
- [14] J. Major, L. Phillips, M. Al Turkestani, L. Bowen, T. Whittles, V. Dhanak, K. Durose, *Sol. Energy Mater. Sol. Cells* **2017**, 172, 1.
- [15] C. H. Don, T. P. Shalvey, M. J. Smiles, L. Thomas, L. J. Phillips, T. D. C. Hobson, H. Finch, L. A. H. Jones, J. E. N. Swallow, N. Fleck, C. Markwell, P. K. Thakur, T.-L. Lee, D. Biswas, L. Bowen, B. A. D. Williamson, D. O. Scanlon, V. R. Dhanak, K. Durose, T. D. Veal, J. D. Major, *Adv. Mater. Interfaces* **2023**, 10, 2300238.
- [16] O. S. Hutter, L. J. Phillips, K. Durose, J. D. Major, *Sol. Energy Mater. Sol. Cells* **2018**, 188, 177.
- [17] H. Shiel, O. S. Hutter, L. J. Phillips, J. E. N. Swallow, L. A. H. Jones, T. J. Featherstone, M. J. Smiles, P. K. Thakur, T.-L. Lee, V. R. Dhanak, J. D. Major, T. D. Veal, *ACS Appl. Energy Mater.* **2020**, 3, 11617.
- [18] T.-Y. Chu, S. Alem, P. G. Verly, S. Wakim, J. Lu, Y. Tao, S. Beaupré, M. Leclerc, F. Bélanger, D. Désilets, S. Rodman, D. Waller, R. Gaudiana, *Appl. Phys. Lett.* **2009**, 95, 063304.
- [19] B. Kim, H. R. Yeom, M. H. Yun, J. Y. Kim, C. Yang, *Macromolecules* **2012**, 45, 8658.
- [20] H. Li, K. Fu, A. Hagfeldt, M. Grätzel, S. G. Mhaisalkar, A. C. Grimsdale, *Angew. Chem., Int. Ed.* **2014**, 53, 4085.
- [21] W. Sachtler, G. Dorgelo, A. Holscher, *Surf. Sci.* **1966**, 5, 221.
- [22] Y. C. Choi, T. N. Mandal, W. S. Yang, Y. H. Lee, S. H. Im, J. H. Noh, S. I. Seok, *Angew. Chem., Int. Ed.* **2014**, 53, 1329.
- [23] D.-B. Li, X. Yin, C. R. Grice, L. Guan, Z. Song, C. Wang, C. Chen, K. Li, A. J. Cimaroli, R. A. Awni, D. Zhao, H. Song, W. Tang, Y. Yan, J. Tang, *Nano Energy* **2018**, 49, 346.
- [24] R. T. Tung, *Phys. Rev. Lett.* **2000**, 84, 6078.
- [25] N. Koch, *Appl. Phys. Lett.* **2021**, 119, 260501.
- [26] H. Ishii, K. Seki, *IEEE Trans. Electron Devices* **1997**, 44, 1295.
- [27] S. Demtsu, J. Sites, *Thin Solid Films* **2006**, 510, 320.
- [28] E. A. Kraut, R. W. Grant, J. R. Waldrop, S. P. Kowalczyk, *Phys. Rev. Lett.* **1980**, 44, 1620.
- [29] H. Shiel, T. D. C. Hobson, O. S. Hutter, L. J. Phillips, M. J. Smiles, L. A. H. Jones, T. J. Featherstone, J. E. N. Swallow, P. K. Thakur, T.-L. Lee, J. D. Major, K. Durose, T. D. Veal, *J. Appl. Phys.* **2021**, 129, 235301.
- [30] D. P. McMeekin, G. Sadoughi, W. Rehman, G. E. Eperon, M. Saliba, M. T. Hörlantner, A. Haghighirad, N. Sakai, L. Korte, B. Rech, M. B. Johnston, L. M. Herz, H. J. Snaith, *Science* **2016**, 351, 151.
- [31] U. B. Cappel, T. Daeneke, U. Bach, *Nano Lett.* **2012**, 12, 4925.
- [32] X. Liu, B. Zheng, L. Shi, S. Zhou, J. Xu, Z. Liu, J. S. Yun, E. Choi, M. Zhang, Y. Lv, W.-H. Zhang, J. Huang, C. Li, K. Sun, J. Seidel, M. He, J. Peng, X. Hao, M. Green, *Nat. Photonics* **2023**, 17, 96.
- [33] T. P. Shalvey, L. J. Phillips, K. Durose, J. D. Major, in *IEEE 7th World Conf. on Photovoltaic Energy Conversion (WCPEC) (A Joint Conference*

- of 45th IEEE PVSC, 28th PVSEC & 34th EU PVSEC), IEEE, New Jersey 2018, pp. 0846–0851.
- [34] H. Hintz, C. Sessler, H. Peisert, H.-J. Egelhaaf, T. Chassé, *Chem. Mater.* **2012**, *24*, 2739.
- [35] M. Manceau, A. Rivaton, J.-L. Gardette, S. Guillerez, N. Lemaître, *Sol. Energy Mater. Sol. Cells* **2011**, *95*, 1315.
- [36] A. L. Fahrenbruch, *MRS Online Proc. Libr.* **2007**, *1012*, 705.
- [37] C. Chen, W. Li, Y. Zhou, C. Chen, M. Luo, X. Liu, K. Zeng, B. Yang, C. Zhang, J. Han, J. Tang, *Appl. Phys. Lett.* **2015**, *107*, 043905.
- [38] D. Bätzner, M. Öszan, D. Bonnet, K. Bücher, *Thin Solid Films* **2000**, *361*, 288.
- [39] N. B. Kotadiya, H. Lu, A. Mondal, Y. Ie, D. Andrienko, P. W. M. Blom, G.-J. A. H. Wetzelaer, *Nat. Mater.* **2018**, *17*, 329.
- [40] N. Fleck, O. S. Hutter, L. J. Phillips, H. Shiel, T. D. C. Hobson, V. R. Dhanak, T. D. Veal, F. Jäckel, K. Durose, J. D. Major, *ACS Appl. Mater. Interfaces* **2020**, *12*, 52595.
- [41] J. Liu, M. D. Bastiani, E. Aydin, G. T. Harrison, Y. Gao, R. R. Pradhan, M. K. Eswaran, M. Mandal, W. Yan, A. Seikhan, M. Babics, A. S. Subbiah, E. Ugur, F. Xu, L. Xu, M. Wang, A. ur Rehman, A. Razzaq, J. Kang, R. Azmi, A. A. Said, F. H. Isikgor, T. G. Allen, D. Andrienko, U. Schwingenschlögl, F. Laquai, S. D. Wolf, *Science* **2022**, *377*, 302.
- [42] Z. Liu, M. Kobayashi, B. C. Paul, Z. Bao, Y. Nishi, in *2009 IEEE International Electron Devices Meeting (IEDM)*, IEEE, New Jersey **2009**, pp. 1–4.